

Probing intrinsic magnon bandgap in a layered hybrid perovskite antiferromagnet by a superconducting resonator

Yi Li,^{1,*} Timothy Draher^{1,2}, Andrew H. Comstock,³ Yuzan Xiong,^{1,4} Md Azimul Haque⁵, Elham Easy,⁶ Jiangchao Qian⁷, Tomas Polakovic⁸, John E. Pearson,¹ Ralu Divan⁹, Jian-Min Zuo,⁷ Xian Zhang,⁶ Ulrich Welp,¹ Wai-Kwong Kwok,¹ Axel Hoffmann⁷, Joseph M. Luther,⁵ Matthew C. Beard,⁵ Dali Sun,^{3,†} Wei Zhang,^{4,‡} and Valentine Novosad^{1,§}

¹Materials Science Division, Argonne National Laboratory, Lemont, Illinois 60439, USA

²Northern Illinois University, Department of Physics, DeKalb Illinois, 60115, USA

³Department of Physics and Organic and Carbon Electronics Laboratory (ORACEL), North Carolina State University, Raleigh, North Carolina 27695 USA

⁴Department of Physics and Astronomy, University of North Carolina, Chapel Hill, North Carolina 27599, USA

⁵Chemistry and Nanoscience Center, National Renewable Energy Laboratory, Golden, Colorado 80401, USA

⁶Department of Mechanical Engineering, Stevens Institute of Technology, Hoboken, New Jersey 07030, USA

⁷Department of Materials Science and Engineering and Materials Research Laboratory, University of Illinois Urbana-Champaign, Urbana, Illinois 61801, USA

⁸Physics Division, Argonne National Laboratory, Lemont, Illinois 60439, USA

⁹Center for Nanoscale Materials, Argonne National Laboratory, Lemont, Illinois 60439, USA



(Received 28 April 2023; accepted 1 September 2023; published 10 October 2023)

Coherent interactions between different magnetic excitations can lead to formation of magnon band gaps and hybrid magnon modes, which can find their applications in magnonic devices and coherent information processing. In this work, we probe the intrinsic magnon band gap of a layered hybrid perovskite antiferromagnet by its strong coupling to a superconducting resonator. The pronounced temperature tunability of the magnon band gap location allows us to set the photon mode within the gap, leading to a reduction of effective magnon-photon coupling and eventually the disappearance of magnon-photon hybridization. When the resonator mode falls into the magnon band gap, the resonator damping rate increases due to the nonzero coupling to the detuned magnon mode. This allows for quantification of the magnon band gap using an analytical model. Our work brings new opportunities in controlling coherent information processing with quantum properties in complex magnetic materials.

DOI: [10.1103/PhysRevResearch.5.043031](https://doi.org/10.1103/PhysRevResearch.5.043031)

I. INTRODUCTION

Hybrid quantum systems [1–3] offer an important pathway for harnessing different natural advantages of complementary quantum systems, leveraging the distinct properties of their constituent excitations. The fundamental excitations of magnetically ordered materials, i.e., magnons, provide efficient coupling with other excitations [4–6], such as microwave photons [7–17] and acoustic phonons [18–21], therefore holding promise for future integration with diverse quantum modules [22–25].

Besides the studies of hybrid magnonics in heterogeneous systems, recent studies of magnon-magnon coupling within

the magnetic media [26–33] show new promise for controlling coherent magnon interactions. In an antiferromagnet or a synthetic antiferromagnet, the acoustic and optic modes, which correspond to the in-phase and out-of-phase precession of the two antiparallel spin sublattices, can intercept each other and form new hybrid modes, leading to their mode splitting or a magnon band gap [28]. This effect can be used for controlling magnetic excitations in unconventional ways, such as magnetically induced transparency [34] and exciting short-wavelength spin waves [35,36]. In addition, the confinement of hybrid magnon modes within the magnetic materials enables their compact integration with microwave circuits and suggest potential applications in magnonic devices such as microwave filters [37] and logic devices [38,39] similar to magnonic crystals [40].

The recent two-dimensional (2D) organic layered magnets [41] offer distinct advantages in their structure-enabled topological chirality and symmetry breaking [42], offering new potentials for hybrid magnonics among other emerging magnetic materials [43–47]. One nice class of materials is 2D magnetic hybrid organic-inorganic perovskites (HOIPs) possessing both superior structural versatility and long-range magnetic order [48–51]. They usually exhibit an interlayer

*yili@anl.gov

†dsun4@ncsu.edu

‡zhwei@unc.edu

§novosad@anl.gov

antiferromagnetic (AFM) coupling [52], inducing the acoustic and optical magnon modes [28,53] in the gigahertz (GHz) frequency range. In addition, the structural symmetry breaking leads to Dzyaloshinskii-Moriya interaction (DMI) [54], causing a finite spin canting [55,56] and creating an intrinsic magnon band gap where the acoustic and optical modes intersect [57]. This is fundamentally different from the magnon band gap induced by an external field [28,30–33,58,59] in that the DMI has provided an intrinsic effective field for magnon-magnon coupling without the need of external field. Furthermore, the large sensitivity of the magnon band gap to small temperature change can lead to new opportunities of modulating magnonic coupling for coherent operations [60–62].

In this Letter, we probe the intrinsic magnon band gap of a 2D HOIPs, $(\text{CH}_3\text{CH}_2\text{NH}_3)_2\text{CuCl}_4$ (Cu-EA) [57], by a coplanar superconducting resonator. The high sensitivity of the superconducting resonator [63] enabled coherent magnon-photon coupling and avoided crossing with a small Cu-EA flake. By changing the temperature of the sample, the location of the DMI-induced magnon band gap can be adjusted so that the resonator photon mode completely falls into the gap and eliminates magnon-photon mode hybridization. At the same time, the magnetic interaction with the resonator causes the resonator linewidth to broaden. Using our developed analytical model, the narrow-band linewidth broadening measurements can be used to extract the magnon band gap, which quantitatively agrees with the broad-band FMR measurements. Our results highlight the opportunity of manipulating coherent mode hybridization with new quantum materials and probing their complex magnonic dispersion with narrow-band microwave characterizations.

II. MATERIAL CHARACTERIZATION

The chemical structure of Cu-EA features corner-sharing halogen (Cl) octahedra with the Cu atom situated at the center, as shown in Fig. 1(a). The canted inorganic CuCl_4 -octahedral structures allow for intralayer long-range magnetic order with superexchange Cu-Cl-Cu interactions, while the interlayer organic cations modulate the interlayer antiferromagnetic (AFM) coupling [52]. Raman spectroscopy of the Cu-EA [64] confirms the vibration modes of the octahedral structure (at 175, 250, and 280 cm^{-1}) and the organic cation (at 100 cm^{-1}) [65], as shown in Fig. 1(c). We have also conducted inductively coupled plasma (IPC) spectroscopy on the sample, showing accurate stoichiometry of the elemental weight as compared with the chemical structure; see the Appendix for details.

Figure 1(d) shows the broad-band ferromagnetic resonance of a large Cu-EA crystal at 1.6 K at parallel pumping condition, i.e., $\mu_0 H_B \parallel h_{\text{rf}}^y$ as illustrated in Fig. 2(b). Both the acoustic and optical modes are measured, which can be formulated as [28]

$$\omega_a = \mu_0 \gamma \sqrt{2H_E(2H_E + M_{\text{eff}})} \frac{H}{2H_E}, \quad (1)$$

$$\omega_o = \mu_0 \gamma \sqrt{2H_E M_{\text{eff}} \left(1 - \frac{H^2}{4H_E^2}\right)}, \quad (2)$$

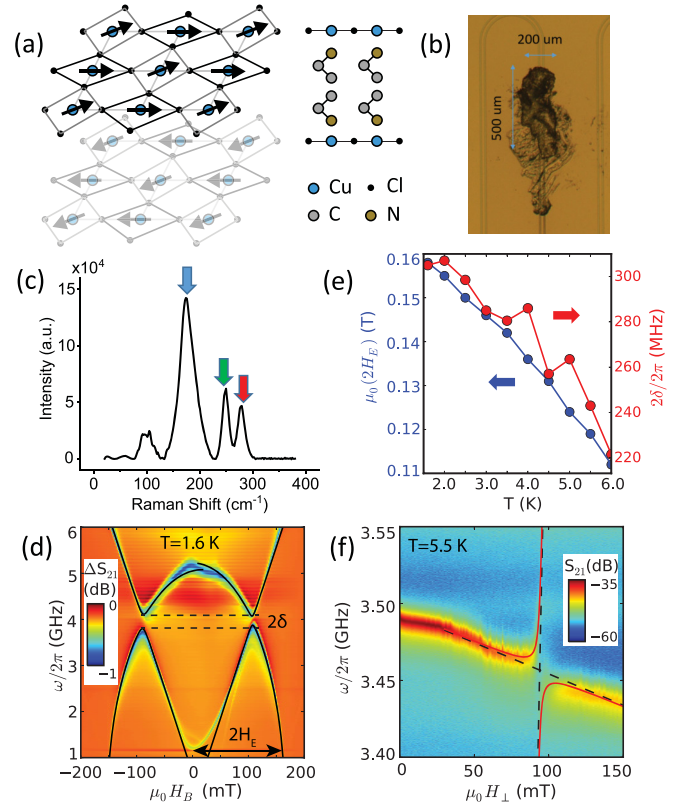


FIG. 1. (a) Lattice structure of layered perovskite antiferromagnet Cu-EA, with Cu filling the octahedral sites of Cl and the antiferromagnetic layers separated by the $\text{CH}_3\text{CH}_2\text{NH}_3$ molecules. (b) Optical microscope image of a small Cu-EA flake mounted onto a CPW superconducting resonator. (c) Raman spectroscopy of Cu-EA showing the high-frequency octahedral modes and the low-frequency organic structure modes. (d) Broad-band ferromagnetic resonance spectra of a large Cu-EA crystal measured at 1.6 K, which is used to extract the magnon band gap 2δ , the interlayer exchange field $2H_E$, and magnon damping rate κ_m . The color bar shows the signals ΔS_{21} after background subtraction. (e) Extracted $2H_E$ (magenta) and 2δ (red) as a function of T . (f) Mode anticrossing between magnons and photons at 5.5 K, with $H_B \perp h_{\text{rf}}^y$. The color bar shows the signals S_{21} in absolute values. The red curves are the fits with $g/2\pi = 45$ MHz. The black dashed lines denote the magnon and photon modes without interaction.

where H_E is the interlayer exchange coupling field, M_{eff} is the effective magnetization which contributes to the perpendicular demagnetization field, and $\gamma/2\pi = (g_e/2) \times 28$ GHz/T is the gyromagnetic ratio, with g_e as the g factor of the magnetization. Clear avoided crossing gaps between the two modes show the existence of magnon band gap around 4 GHz. The coupled magnon spectra can be fitted to the hybrid mode expression $\omega_{\pm}^{mm} = (\omega_a + \omega_o)/2 \pm \sqrt{(\omega_a - \omega_o)^2/4 + \delta^2}$, where δ is the magnon-magnon coupling strength. The fitting curves are plotted in Fig. 1(d). The extracted parameters are $\mu_0 H_E = 0.16$ T, $\mu_0 M_{\text{eff}} = 80$ mT, $g_e = 2.3$, and $\delta/2\pi = 150$ MHz. Note that the actual saturation magnetization of Cu-EA can be larger than M_{eff} because the shape of the sample crystal is not a perfect two-dimension system and the perpendicular demagnetization factor can be smaller than one. The strong magnon-magnon coupling observed in Cu-EA at par-

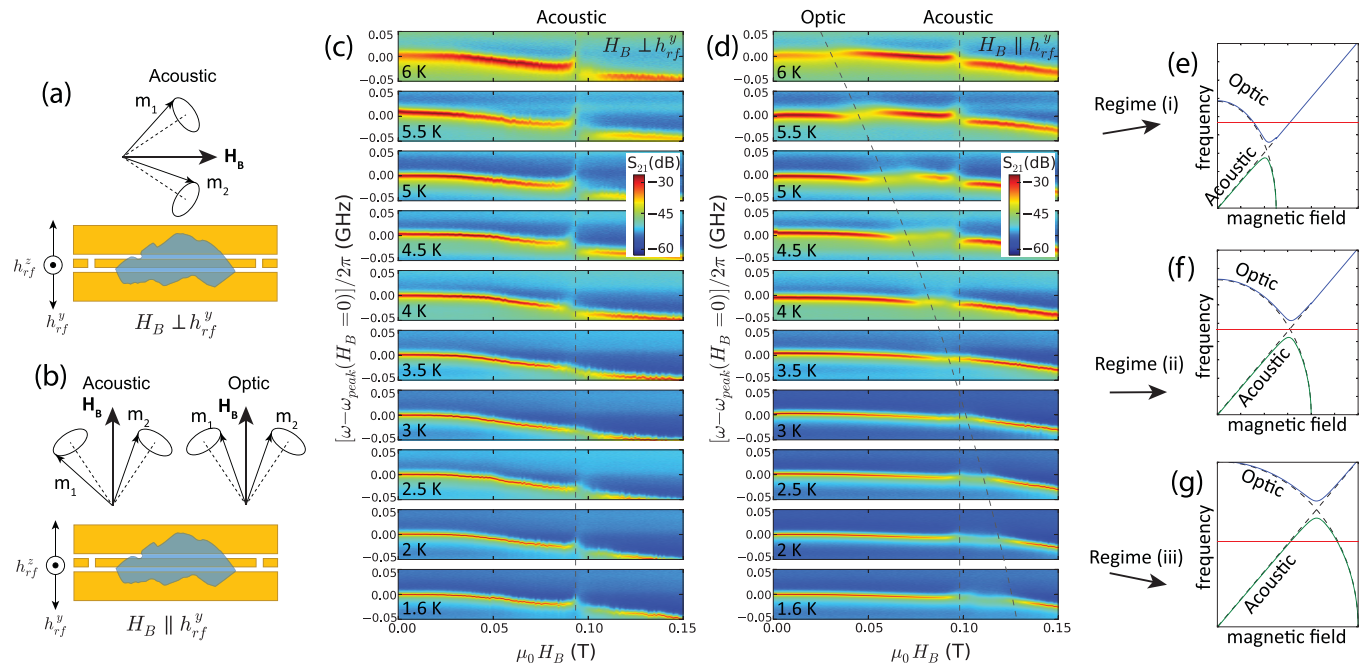


FIG. 2. (a), (b) Illustration of two different in-plane field alignments and their selective mode excitations. In (a), $\mu_0 H_B \perp h_{rf}^y$ and only the acoustic mode is excited. In (b), $\mu_0 H_B \parallel h_{rf}^y$ and both the acoustic and optical modes are excited. (c), (d) Temperature dependence of the magnon-photon coupling evolutions from 1.5 to 6 K with two different magnetic field alignments. All the dispersion centered at the resonator photon mode ($\omega_p/2\pi \approx 3.5$ GHz). Dashed curves are guide to eye for the acoustic mode crossing the resonator mode at $\mu_0 H_a = 95$ mT and the optical mode crossing the resonator mode at different fields. (e)–(g) Illustration of the three regimes where the resonator mode is (e) above, (f) within, and (g) below the magnon band gap.

allel pumping condition, which is absent in other layered [28] or synthetic [30,31] antiferromagnets at the same pumping condition, is caused by the spontaneous canting of the octahedral CuCl_4^{2-} spin sites from their chiral DMI and the resultant overlap between the acoustic and optical modes [57]. Figure 1(e) shows the temperature dependence of extracted $2H_E$ and the magnon band gap 2δ from Fig. 1(d). With the same y-axis proportion ratio in Fig. 1(e), a good overlap of H_E and δ shows that they are proportional to each other at different temperatures. This suggests that the DMI-induced spin canting shares a similar mechanism with the interlayer exchange coupling in Cu-EA. The magnon damping rate, κ_m , of the acoustic and optical modes are also extracted and are found to be weakly frequency and temperature dependent. In the range of 2–5 GHz, $\kappa_m/2\pi \sim 50$ MHz for the acoustic mode and ~ 80 MHz for the optical mode.

III. MAGNON-PHOTON COUPLING

To feature the sensitivity of the superconducting resonator to small magnetic crystals, we precisely transfer a thin Cu-EA flake with lateral dimensions of $500 \mu\text{m} \times 200 \mu\text{m}$ and a thickness of $40 \mu\text{m}$ onto the center of a half-wavelength NbN coplanar wave guide (CPW) superconducting resonator with a signal line width of $20 \mu\text{m}$, as shown in Fig. 1(b). The dimension matching between the signal line and the flake thickness allows for optimal coupling of the magnon excitations to the resonator. The loaded superconducting resonator exhibits a sharp peak at $\omega_p/2\pi = 3.5$ GHz and a zero-field half-width half-maximum linewidth of $\kappa_p/2\pi = 0.4$ MHz at

1.6 K, which corresponds to a quality factor of $\omega_p/2\kappa_p = 4400$.

The maximum mode splitting happens at 5.5 K between the acoustic magnon mode of Cu-EA and the resonator photon mode, shown in Fig. 1(f). The peak positions of the avoided crossing can be fitted to the hybrid modes [7]:

$$\omega_{\pm}^{mp} = (\omega_m + \omega_p)/2 \pm \sqrt{(\omega_m - \omega_p)^2/4 + g^2}, \quad (3)$$

where ω_m is the magnon frequency, ω_p is the photon frequency, and g is the magnon-photon coupling strength due to dipolar interaction. The field dependence of ω_p can be extracted from the linear extrapolation of the background, and the field dependence of ω_m can be obtained from the broadband FMR spectrum. Fits to Eq. (3) yield $g/2\pi = 45$ MHz. Using the damping rates of $\kappa_p/2\pi = 2.7$ MHz for the superconducting resonator at 5.5 K and $\kappa_m/2\pi = 50$ MHz for the Cu-EA acoustic mode, we obtain a cooperativity of $C = g^2/\kappa_p\kappa_m = 15$. We note that even though the cooperativity becomes higher at lower temperature, e.g., 1.6 K, because of the much lower κ_p , the real bottleneck of strong magnon-photon coupling is the ratio g/κ_m , which is maximized as 0.95 at 5.5 K. The strong coupling regime requires both g/κ_m and g/κ_p to be greater than one [10].

IV. MODULATION OF MAGNON-PHOTON COUPLING AT DIFFERENT TEMPERATURES

Next, we investigate the temperature dependence of the magnon-photon interactions. Shown in Figs. 2(a) and 2(b),

the signal line of the resonator generates both the in-plane and perpendicular Oersted fields, h_{rf}^y and h_{rf}^z , respectively. In the orthogonal pumping condition ($\mu_0 H_B \perp h_{rf}^y$), the Oersted field components h_{rf}^y and h_{rf}^z only couple to the acoustic mode. In the parallel pumping condition ($\mu_0 H_B \parallel h_{rf}^y$), h_{rf}^y couples to the acoustic mode and h_{rf}^z couples to the optical mode. Thus, the field alignment allows for selective excitation of the acoustic mode in Fig. 2(c), or the mutual excitation of both modes in Fig. 2(d). The interaction with the acoustic mode is manifested by an avoided crossing at a constant field of $\mu_0 H_a = 95$ mT for both pumping geometries. The optical mode found in Fig. 2(d) shows a large temperature-dependent drift of its location, as marked by the dashed curves. The reversed anticrossing compared with the acoustic mode shows that the magnon frequency decreases as the field rises, agreeing with the feature of the optical mode as shown in Fig. 1(d).

Due to the tunability of H_E , the center frequency of the magnon band gap changes rapidly with temperature in the range from 1.5 to 6.0 K, therefore, allowing the resonator mode (much less sensitive to temperature) to intercept with the magnon band gap while maintaining a nearly constant quality factor. Three regimes of the magnon-photon coupling between the Cu-EA flake and the superconducting resonator are observed, with the relation between the magnon band gap and the resonator mode shown in Figs. 2(e)–2(g). In regime (i) ($T > 3.5$ K), the magnon band gap is below the superconducting resonator frequency [Fig. 2(e)]. The resonator photon mode coherently interacts with the acoustic mode in Fig. 2(c), and both the acoustic and optical modes in Fig. 2(d). In regime (ii) ($3.5 \geq T \geq 3$ K), the acoustic and optical magnon modes cross each other and form the magnon band gap at the superconducting resonator mode frequency. This causes the resonator mode to fall inside the magnon band gap, leading to a moderate change of the peak amplitude and linewidth without peak frequency shift around 95 mT. In regime (iii) ($T < 3$ K), where the magnon band gap is above the resonator mode, the acoustic mode resumes its anticrossinglike interaction with the resonator mode. In addition, for the $\mu_0 H_B \parallel h_{rf}^y$ geometry where the optical mode also interacts with the resonator mode [Fig. 2(d)], the regime between the optical and acoustic modes are blurred, as shown in regimes (i) and (iii). This indicates that one of the two acoustic-optical hybrid magnonic modes is still near the resonator mode and maintains the magnon-photon interaction.

Figure 3 summarizes extracted magnon-photon coupling strength, g , as a function of T . To verify the phenomena, we have also coupled another Cu-EA crystal to a lumped-element resonator (LER) [66]. This allows for a larger magnon-photon coupling strength while maintaining the same magnon band gap. For both the CPW resonator and LER, g quickly decreases in regime (ii) due to mode degeneracy breaking between the magnon mode and the resonator photon mode. The zero coupling strength for the CPW resonator is manifested by the continuous evolution of resonator peak without mode anticrossing, as shown in Figs. 2(c) and 2(d). For the LER, a finite g can still be extracted in regime (ii) which is due to nonperfect centering of the resonator mode in the magnon band gap when then magnon-photon coupling is large. The maximal acoustic mode coupling strengths for the

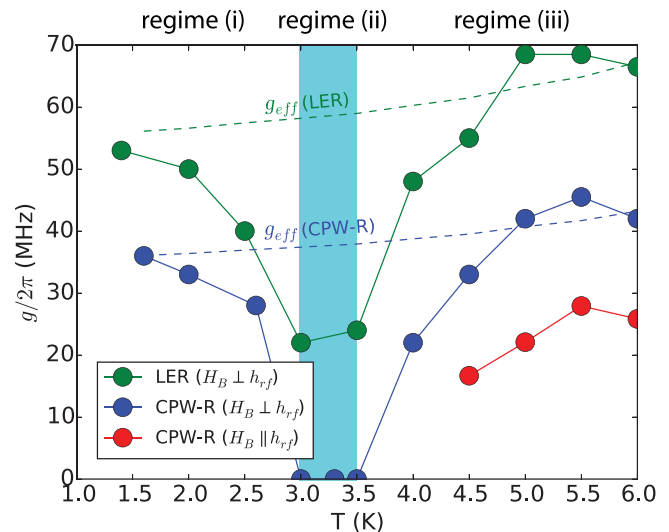


FIG. 3. Extracted effective magnon-photon coupling g as a function of T . The resonator mode is within the magnon band gap between 3 and 3.5 K, yielding $g = 0$.

CPW resonator are $g_{\text{CPW}}^{\perp}/2\pi = 45$ MHz for $\mu_0 H_B \perp h_{rf}^y$ and $g_{\text{CPW}}^{\parallel}/2\pi = 28$ MHz for $\mu_0 H_B \parallel h_{rf}^y$ at 5.5 K. Their difference quantifies the coupling ratio of the acoustic magnon mode between the in-plane (h_{rf}^y) and perpendicular (h_{rf}^z) Oersted fields from the CPW: at $\mu_0 H_B \perp h_{rf}$, both h_{rf}^y and h_{rf}^z couple to the acoustic mode, while at $\mu_0 H_B \parallel h_{rf}$, only h_{rf}^z couples to the acoustic mode. The ratio can be calculated as $h_{rf}^y/h_{rf}^z = \sqrt{(g_{\text{CPW}}^{\perp})^2 - (g_{\text{CPW}}^{\parallel})^2}/g_{\text{CPW}}^{\perp} = 1.25$. For the LER, the obtained ratio is 1.23. This suggests that h_{rf}^z plays an important role in magnon-photon coupling. When the magnon band gap is far from the resonator mode (e.g., 1.5 K and 6 K), a reduction of g from 6 K to 1.5 K reflects the change of coupling efficiency between the Oersted field and the canted magnetization at different biasing field directions. We plot the calculated prediction of the effective magnon-photon coupling, g_{eff} , for the acoustic magnon mode without considering the magnon band gap, and the trend nicely captures the experiment at low and high temperatures.

V. EXTRACTION OF MAGNON BAND GAP BY DAMPING ENHANCEMENT

We show that the magnon band gap of Cu-EA can be quantitatively extracted from the modulated magnon-photon interaction. When the resonator mode is inside the magnon band gap in regime (ii), the interaction between the magnon and photon modes leads to a linewidth broadening of the resonator photon mode, as shown in Fig. 4(a). Such an effect has been previously observed in magnon-magnon coupled bilayers in the Purcell regime [34,35,67,68]. We develop an analytical model for quantifying the change of photon linewidth by considering two detuned magnon modes coupled to the photon mode. The photon damping rate κ_c can be expressed as

$$\kappa_c = \kappa_{c0} + (g_{\text{eff}})^2 \frac{\kappa_m}{\kappa_m^2 + \delta^2}, \quad (4)$$

where κ_{c0} is the intrinsic photon damping rate, g_{eff} is the effective magnon-photon coupling strength as plotted in Fig. 3, κ_m is the magnon damping rate, and 2δ is the magnon-magnon band gap. The detailed derivation of the model is discussed in the Appendix. Note that the information of g_{eff} needs to be obtained from regime (iii) where mode anticrossing between the magnon and photon modes are resumed. Equation (4) shows that the change of linewidth $\Delta\kappa_c = \kappa_c - \kappa_{c0}$ is proportional to $(g_{\text{eff}})^2$, with the slope determined by two intrinsic magnon characteristics of the Cu-EA: κ_m and 2δ . With two completely different superconducting resonator designs, i.e., the CPW resonator and LER, we find that the extracted $\Delta\kappa_c$ nicely follows the linear dependence of $(g_{\text{eff}})^2$, shown in Fig. 4(b), with a slope of $(210 \text{ MHz})^{-1}$. For κ , we take the average of the acoustic and optical modes, as $\kappa_m/2\pi = 65 \text{ MHz}$. The magnon band gap is calculated to be $\delta/2\pi = 152 \text{ MHz}$, which is close to the value in Fig. 1(e) as 140 MHz around 3.5 K . Thus, we confirm the validity of this new technique for quantifying the magnon band gap δ of a small magnetic flake with a highly sensitive superconducting microwave resonator, where the linewidth change of the resonator mode acts as a probe to interact with the acoustic-optical hybrid magnon modes.

VI. CONCLUSION

In summary, we have probed the intrinsic magnon band gap in a layered perovskite antiferromagnet using its strong coupling with a superconducting resonator. The use of high-quality-factor superconducting resonator allows for coherent interaction with the magnon excitations and the study of magnon band gap with narrow-band microwave measurements. The magnon-photon coupling strength can be tuned from a few tens of megahertz to zero by modifying the magnon band gap location with temperature. At the zero coupling strength state where the resonator mode falls into the magnon band gap, probing the change of photon mode linewidth also allows one to extract the value of magnon band gap using an analytical model. Our results provide a new approach to study the quantum properties of novel layered magnetic materials from cavity magnonics. The controllability of effective magnon-photon coupling strength may also find potential in magnonic gate operations [61,69,70]. To improve the slow temperature tunability of magnon band gap, we anticipate other approaches such as strain or electric field [71–73] for controlling the magnetic properties with high speed and extending the application in coherent information processing.

ACKNOWLEDGMENTS

D.S. and M.B. acknowledge the primary financial support through the Center for Hybrid Organic Inorganic Semiconductors for Energy (CHOISE), an Energy Frontier Research Center funded by the Office of Basic Energy Sciences, Office of Science within the U.S. Department of Energy (Hybrid perovskite synthesis, crystal preparation, structural characterization, and motivation of this work). This work was authored in part by the National Renewable Energy Laboratory (NREL), operated by the Alliance for Sustainable Energy LLC, for the U.S. Department of Energy (DOE) under

Contract No. DE-AC36-08GO28308. The views expressed in this article do not necessarily represent the views of the DOE or the U.S. Government. Works at Argonne National Laboratory and University of Illinois and Urbana-Champaign, including the superconducting resonator fabrication, design, ICP chemical analysis, and hybrid magnonics characterization, were supported by the U.S. DOE, Office of Science, Basic Energy Sciences, Materials Sciences and Engineering Division under Contract No. DE-SC0022060. Work at UNC-CH were supported by NSF-ECCS 2246254 for the experimental design, data analysis, theoretical analysis, and manuscript preparation. D.S. acknowledges the partial financial support from the Department of Energy Grant No. DE-SC0020992 and the National Science Foundation Grant No. DMR-2143642 for magnetic properties characterization. X.Z. acknowledges support by the National Science Foundation CAREER Award (Grant No. CBET-2145417) and LEAPS Award (Grant No. DMR-2137883) for the Raman characterization. Use of the Center for Nanoscale Materials (CNM), an Office of Science user facility, was supported by the U.S. Department of Energy, Office of Science, Office of Basic Energy Sciences, under Contract No. DE-AC02-06CH11357.

APPENDIX

1. Sample and device preparation

Stoichiometric ratios of Copper (II) chloride dihydrate ($\text{CuCl}_2 \cdot 2\text{H}_2\text{O}$), aqueous ethylamine, and hydrochloric acid were mixed and heated to 100°C while stirring. After the solution was prepared, it was removed from the hot plate and cooled to room temperature. The flakes of Cu-EA were isolated by vacuum filtration. The superconducting resonators were fabricated using NbN(200 nm) thin films grown on Si substrates and reactive ion etching (RIE). Figure 5 shows the optical microscope images of the CPW resonator and the lumped element resonator (LER). The CPW resonator is a half-wavelength resonator with two open nodes on the top and bottom side of the CPW. The LER consists of a large interdigital transducer-like (IDT) capacitor array shorted by a wire in the middle of the IDT array, forming an LC resonator with a large capacitance (C) and a small inductance (L) to provide high sensitivity to spin excitations. The two resonators are designed so that their eigenfrequencies are around 3.5 GHz to match the magnon band gap location of Cu-EA. The sizes of the Cu-EA crystals are $500 \times 200 \mu\text{m}^2$ for the CPW resonator and $300 \times 200 \mu\text{m}^2$ on the LER. They are mounted onto the superconducting resonators for being inductively coupled to the superconducting resonator photons.

2. Raman and Inductively Coupled Plasma spectroscopy of Cu-EA

A micro Raman spectrometer (RENISHAW inVia Raman microscope system) was used for the spectroscopy measurement of Cu-EA crystal from 10 to 3000 cm^{-1} with a 532 nm wave length laser and a laser spot size of $0.26 \mu\text{m}$. The low-frequency spectrum ($\leq 500 \text{ cm}^{-1}$) has a much stronger amplitude than the high-frequency spectrum ($\geq 500 \text{ cm}^{-1}$). Only the low-frequency spectrum is shown in the main text.

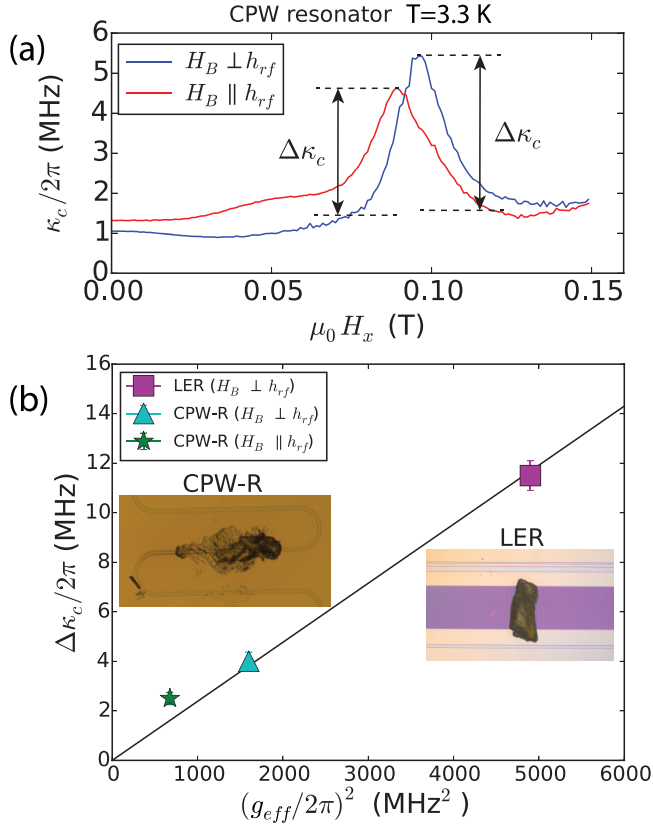


FIG. 4. (a) Superconducting resonator linewidth κ_c as a function of H_B at $T = 3.3$ K, where the resonator mode is inside the magnon band gap. (b) SC resonator linewidth change $\Delta\kappa_c$ as a function of g_{eff}^2 for the CPW and LER resonator designs. Error bars denote the uncertainty of base resonator linewidth drift under external magnetic fields. The red line is a fit to Eq. (4), with the slope quantifying the magnon band gap 2δ .

For the inductively coupled plasma (ICP) analysis, we took a piece of Cu-EA crystal with a total weight of 2.7 mg. The crystal was combusted into gas, and subsequently

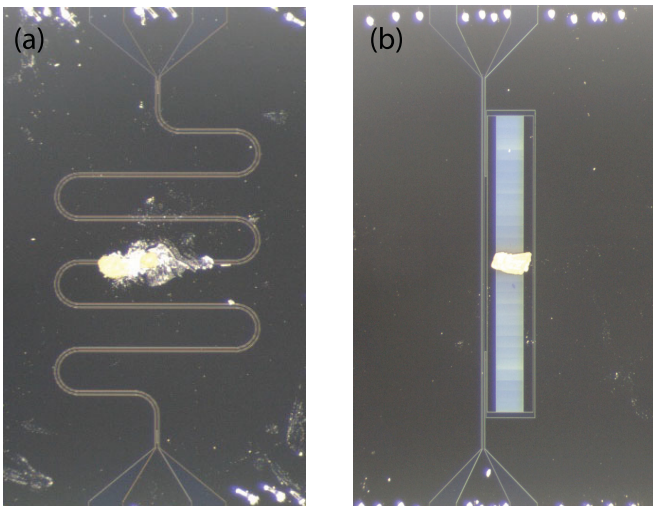


FIG. 5. Optical microscope images of (a) the CPW resonator and (b) the lumped-element resonator mounted with Cu-EA crystals.

TABLE I. Elemental testing results of $(\text{CH}_3\text{CH}_2\text{NH}_3)_2\text{CuCl}_4$ crystals.

Element	Theory	Exp	Difference
C, H, N element test			
C	16.15%	17.35%	1.20%
H	5.42%	5.28%	-0.14%
N	9.41%	9.66%	0.25%
Halide test			
Cl	47.66%	46.01%	-1.65%
ICP test			
Cu	21.36%	19.38%	-1.98%

absorbed into a solution. A combination of three techniques was performed to determine the elemental composition in the Microanalysis Lab, Chemistry Department, UIUC. The carbon, hydrogen, and nitrogen content were quantitatively determined by CHN analysis using an Exeter Analytical CE440 CHN Analyzer. The copper content was measured by ICP-MS analysis on a Perkin-Elmer NexION 350D ICP-MS instrument. The determination of chlorine (Cl) was done using an ion-selective electrode (ISE) method (thermo scientific orion ion selective electrodes, chlorine combination probe). The results are shown in Table I, where the elemental weight percentages agree well with the composition of Cu-EA, or $(\text{CH}_3\text{CH}_2\text{NH}_3)_2\text{CuCl}_4$, with the differences less than 2%.

3. Temperature dependence of g_{eff}

In Fig. 3, the value of g_{eff} is calculated as the mutual effects of h_{rf}^y and h_{rf}^z :

$$g_{\text{eff}} = \sqrt{(g_0^y \cos \theta)^2 + (g_0^z)^2}, \quad (\text{A1})$$

where $\theta = \cos^{-1}(H_a/2H_E)$ is the angle between the canted magnetization and the biasing field H_a , g_0^y is the effective coupling strength between the magnetization and h_{rf}^y (maximized when the magnetization is saturated as being parallel to the biasing field and orthogonal to h_{rf}^y), and g_0^z is the effective coupling strength between the magnetization and h_{rf}^z . The values of g_0^y and g_0^z can be calculated from the extracted values of g at 6.0 K. For CPW-R in Fig. 3, we obtain $g_{\text{eff}}/2\pi = \sqrt{(g_0^y)^2 + (g_0^z)^2}/2\pi = 45$ MHz for $H_B \perp h_{rf}^y$, and $g_{\text{eff}}/2\pi = g_0^z/2\pi = 28$ MHz for $H_B \parallel h_{rf}^y$. Thus, $g_0^y/2\pi = \sqrt{45^2 - 28^2} = 35$ MHz. For LER, we obtain $g_{\text{eff}}/2\pi = \sqrt{(g_0^y)^2 + (g_0^z)^2}/2\pi = 68$ MHz for $H_B \perp h_{rf}^y$, and $g_{\text{eff}}/2\pi = g_0^z/2\pi = 42$ MHz for $H_B \parallel h_{rf}^y$. Thus, $g_0^y/2\pi = \sqrt{68^2 - 42^2} = 53$ MHz. By using $\mu_0 H_a = 94$ mT for the acoustic mode and the temperature dependence of $2H_E$ as plotted in Fig. 1(e) of the main text, we can plot $g_{\text{eff}}(T)$ as the dashed curves in Fig. 3. This dependence explains the drift of g_{eff} measured at the condition of $H_B \perp h_{rf}^y$ as the temperature decreases.

4. Derivation of coupling-induced resonator linewidth broadening

When the resonator mode sits at the center of the magnon band gap, the evolution of the microwave transmission

spectrum can be formulated as

$$t(\omega) = \frac{2\kappa_a}{i(\omega - \omega_c) + \kappa_{c0} + \frac{(g_{hyb})^2}{i(\omega - \omega_{m1}) + \kappa_{m1}} + \frac{(g_{hyb})^2}{i(\omega - \omega_{m2}) + \kappa_{m2}}}. \quad (\text{A2})$$

In Eq. (A2), κ_a is the external coupling between the resonator to the microwave transmission line, ω_c and κ_{c0} are the eigenfrequency and damping rate of the resonator, respectively. Both the upper and lower hybrid magnon branches couple to the resonator mode with the same coupling strength (g_{hyb}). We assume they have the same damping, $\kappa_{m1} = \kappa_{m2} = \kappa_m$, and their frequencies are off the resonator mode by half the magnon band gap (δ), as $\omega_{m1} = \omega_c + \delta$ and $\omega_{m2} = \omega_c - \delta$. The total damping of the resonator at $\omega = \omega_c$ can be calculated from the denominator of Eq. (S5):

$$\kappa_c = \kappa_{c0} + \frac{(g_{hyb})^2}{i\delta + \kappa_m} + \frac{(g_{hyb})^2}{-i\delta + \kappa_m} = \kappa_{c0} + \frac{2(g_{hyb})^2\kappa_m}{\kappa_m^2 + \delta^2}. \quad (\text{A3})$$

Note that when the acoustic and optical magnon modes are degenerate in frequency, as is the case at the center of the magnon band gap, the two hybrid magnon modes are the in-phase and out-of-phase combination of the acoustic and

optical components and their weights are 50:50 in the mode contribution. The coupling strength g_{hyb} , which is a weighed sum of the acoustic and optical coupling strength, can be calculated accordingly. In the case of $H_B \perp h_{rf}^y$, the optical mode does not couple to the Oersted field, and the acoustic mode exhibit a coupling strength of g_{eff} as denoted in the previous section. Thus, we have $g_{hyb} = g_{eff}/\sqrt{2}$ and the factor of two in Eq. (A3) is canceled:

$$\kappa_c = \kappa_{c0} + \frac{(g_{hyb})^2\kappa_m}{\kappa_m^2 + \delta^2}, \quad (\text{A4})$$

which is the same as Eq. (2) of the main text.

In the case of $H_B \parallel h_{rf}^y$, the situation is more complicated as both the acoustic and optical modes couple to the Oersted field. This explains the deviation of the $\Delta\kappa$ - g^2 linear dependence in Fig. 4 of the main text. However, the total Oersted field is the same. The energy transfer between the Oersted field and the hybrid magnon mode is simply shifted from going through the acoustic mode to going through both the acoustic and optical modes. Thus, in this case, g_{hyb} should be close to $g_{eff}/\sqrt{2}$, and Eq. (A4) is still a valid representation of Eq. (A3).

-
- [1] G. Kurizki, P. Bertet, Y. Kubo, K. Mølmer, D. Petrosyan, P. Rabl, and J. Schmiedmayer, Quantum technologies with hybrid systems, *Proc. Natl. Acad. Sci. USA* **112**, 3866 (2015).
- [2] A. A. Clerk, K. W. Lehnert, P. Bertet, J. R. Petta, and Y. Nakamura, Hybrid quantum systems with circuit quantum electrodynamics, *Nat. Phys.* **16**, 257 (2020).
- [3] D. Lachance-Quirion, Y. Tabuchi, A. Glorpe, K. Usami, and Y. Nakamura, Hybrid quantum systems based on magnonics, *Appl. Phys. Express* **12**, 070101 (2019).
- [4] Y. Li, W. Zhang, V. Tyberkevych, W.-K. Kwok, A. Hoffmann, and V. Novosad, Hybrid magnonics: physics, circuits and applications for coherent information processing, *J. Appl. Phys.* **128**, 130902 (2020).
- [5] Y. Li, C. Zhao, W. Zhang, A. Hoffmann, and V. Novosad, Advances in coherent coupling between magnons and acoustic phonons, *APL Mater.* **9**, 060902 (2021).
- [6] X. Zhang, A review of common materials for hybrid quantum magnonics, *Mater. Today Electron.* **5**, 100044 (2023).
- [7] H. Huebl, C. W. Zollitsch, J. Lotze, F. Hocke, M. Greifenstein, A. Marx, R. Gross, and S. T. B. Goennenwein, High cooperativity in coupled microwave resonator ferrimagnetic insulator hybrids, *Phys. Rev. Lett.* **111**, 127003 (2013).
- [8] M. Goryachev, W. G. Farr, D. L. Creedon, Y. Fan, M. Kostylev, and M. E. Tobar, High-cooperativity cavity QED with magnons at microwave frequencies, *Phys. Rev. Appl.* **2**, 054002 (2014).
- [9] Y. Tabuchi, S. Ishino, T. Ishikawa, R. Yamazaki, K. Usami, and Y. Nakamura, Hybridizing ferromagnetic magnons and microwave photons in the quantum limit, *Phys. Rev. Lett.* **113**, 083603 (2014).
- [10] X. Zhang, C.-L. Zou, L. Jiang, and H. X. Tang, Strongly coupled magnons and cavity microwave photons, *Phys. Rev. Lett.* **113**, 156401 (2014).
- [11] L. Bai, M. Harder, Y. P. Chen, X. Fan, J. Q. Xiao, and C.-M. Hu, Spin pumping in electro-dynamically coupled magnon-photon systems, *Phys. Rev. Lett.* **114**, 227201 (2015).
- [12] M. Harder, Y. Yang, B. M. Yao, C. H. Yu, J. W. Rao, Y. S. Gui, R. L. Stamps, and C.-M. Hu, Level attraction due to dissipative magnon-photon coupling, *Phys. Rev. Lett.* **121**, 137203 (2018).
- [13] Y. Li, T. Polakovic, Y.-L. Wang, J. Xu, S. Lendinez, Z. Zhang, J. Ding, T. Khaire, H. Saglam, R. Divan, J. Pearson, W.-K. Kwok, Z. Xiao, V. Novosad, A. Hoffmann, and W. Zhang, Strong coupling between magnons and microwave photons in on-chip ferromagnet-superconductor thin-film devices, *Phys. Rev. Lett.* **123**, 107701 (2019).
- [14] J. T. Hou and L. Liu, Strong coupling between microwave photons and nanomagnet magnons, *Phys. Rev. Lett.* **123**, 107702 (2019).
- [15] B. Bhoi, B. Kim, S.-H. Jang, J. Kim, J. Yang, Y.-J. Cho, and S.-K. Kim, Abnormal anticrossing effect in photon-magnon coupling, *Phys. Rev. B* **99**, 134426 (2019).
- [16] Y.-P. Wang, J. W. Rao, Y. Yang, P.-C. Xu, Y. S. Gui, B. M. Yao, J. Q. You, and C.-M. Hu, Nonreciprocity and unidirectional invisibility in cavity magnonics, *Phys. Rev. Lett.* **123**, 127202 (2019).
- [17] I. Boverter, C. Dörfinger, T. Wolz, R. Macêdo, R. Lebrun, M. Kläui, and M. Weides, Control of the coupling strength and linewidth of a cavity magnon-polariton, *Phys. Rev. Res.* **2**, 013154 (2020).
- [18] T. Kikkawa, K. Shen, B. Flebus, R. A. Duine, K.-ichi Uchida, Z. Qiu, G. E. W. Bauer, and E. Saitoh, Magnon polarons in the spin Seebeck effect, *Phys. Rev. Lett.* **117**, 207203 (2016).
- [19] C. Berk, M. Jaris, W. Yang, S. Dhuey, S. Cabrini, and H. Schmidt, Strongly coupled magnon-phonon dynamics in a single nanomagnet, *Nat. Commun.* **10**, 2652 (2019).

- [20] K. An, A. N. Litvinenko, R. Kohno, A. A. Fuad, V. V. Naletov, L. Vila, U. Ebels, G. de Loubens, H. Hurdequint, N. Beaulieu, J. Ben Youssef, N. Vukadinovic, G. E. W. Bauer, A. N. Slavina, V. S. Tiberkevich, and O. Klein, Coherent long-range transfer of angular momentum between magnon Kittel modes by phonons, *Phys. Rev. B* **101**, 060407(R) (2020).
- [21] J. Xu, C. Zhong, X. Zhou, X. Han, D. Jin, S. K. Gray, L. Jiang, and X. Zhang, Coherent pulse echo in hybrid magnonics with multimode phonons, *Phys. Rev. Appl.* **16**, 024009 (2021).
- [22] M. Harder and C.-M. Hu, Cavity spintronics: An early review of recent progress in the study of magnon-photon level repulsion, *Solid State Phys.* **69**, 47 (2018).
- [23] D. D. Awschalom, C.H.R. Du, R. He, J. Heremans, A. Hoffmann, J. Hou, H. Kurebayashi, Y. Li, L. Liu, V. Novosad, J. Sklenar, S. Sullivan, D. Sun, H. Tang, V. Tyberkevych, C. Trevillian, A. W. Tsen, L. Weiss, W. Zhang, X. Zhang *et al.*, Quantum engineering with hybrid magnonics systems and materials, *IEEE Trans. Quantum Eng.* **2**, 5500836 (2021).
- [24] M. Fukami, D. R. Candido, D. D. Awschalom, and M. E. Flatté, Opportunities for long-range magnon-mediated entanglement of spin qubits via on- and off-resonant coupling, *PRX Quantum* **2**, 040314 (2021).
- [25] H. Y. Yuan, Y. Cao, A. Kamra, R. A. Duine, and P. Yan, Quantum magnonics: When magnon spintronics meets quantum information science, *Phys. Rep.* **965**, 1 (2022).
- [26] S. Klingler, V. Amin, S. Geprägs, K. Ganzhorn, H. Maier-Flaig, M. Althammer, H. Huebl, R. Gross, R. D. McMichael, M. D. Stiles, S. T. B. Goennenwein, and M. Weiler, Spin-torque excitation of perpendicular standing spin waves in coupled YIG/Co heterostructures, *Phys. Rev. Lett.* **120**, 127201 (2018).
- [27] J. Chen, C. Liu, T. Liu, Y. Xiao, K. Xia, G. E. W. Bauer, M. Wu, and H. Yu, Strong interlayer magnon-magnon coupling in magnetic metal-insulator hybrid nanostructures, *Phys. Rev. Lett.* **120**, 217202 (2018).
- [28] D. MacNeill, J. T. Hou, D. R. Klein, P. Zhang, P. Jarillo-Herrero, and L. Liu, Gigahertz frequency antiferromagnetic resonance and strong magnon-magnon coupling in the layered crystal CrCl_3 , *Phys. Rev. Lett.* **123**, 047204 (2019).
- [29] Y. Li, W. Cao, V. P. Amin, Z. Zhang, J. Gibbons, J. Sklenar, J. Pearson, P. M. Haney, M. D. Stiles, W. E. Bailey, V. Novosad, A. Hoffmann, and W. Zhang, Coherent spin pumping in a strongly coupled magnon-magnon hybrid system, *Phys. Rev. Lett.* **124**, 117202 (2020).
- [30] Y. Shiota, T. Taniguchi, M. Ishibashi, T. Moriyama, and T. Ono, Tunable magnon-magnon coupling mediated by dynamic dipolar interaction in synthetic antiferromagnets, *Phys. Rev. Lett.* **125**, 017203 (2020).
- [31] A. Sud, C. W. Zollitsch, A. Kamimaki, T. Dion, S. Khan, S. Iihama, S. Mizukami, and H. Kurebayashi, Tunable magnon-magnon coupling in synthetic antiferromagnets, *Phys. Rev. B* **102**, 100403 (2020).
- [32] J. Sklenar and W. Zhang, Self-Hybridization and tunable magnon-magnon coupling in van der Waals synthetic magnets, *Phys. Rev. Appl.* **15**, 044008 (2021).
- [33] M. Li, J. Lu, and W. He, Symmetry breaking induced magnon-magnon coupling in synthetic antiferromagnets, *Phys. Rev. B* **103**, 064429 (2021).
- [34] Y. Xiong, J. Inman, Z. Li, K. Xie, R. Bidthanapally, J. Sklenar, P. Li, S. Louis, V. Tyberkevych, H. Qu, Z. Xiao, W. K. Kwok, V. Novosad, Y. Li, F. Ma, and W. Zhang, Tunable magnetically induced transparency spectra in magnon-magnon coupled $\text{Y}_3\text{Fe}_5\text{O}_{12}$ /permalloy bilayers, *Phys. Rev. Appl.* **17**, 044010 (2022).
- [35] J. Inman, Y. Xiong, R. Bidthanapally, S. Louis, V. Tyberkevych, H. Qu, J. Sklenar, V. Novosad, Y. Li, X. Zhang, and W. Zhang, Hybrid magnonics for short-wavelength spin waves facilitated by a magnetic heterostructure, *Phys. Rev. Appl.* **17**, 044034 (2022).
- [36] J. Chen, T. Yu, C. Liu, T. Liu, M. Madami, K. Shen, J. Zhang, S. Tu, M. Shah Alam, K. Xia, M. Wu, G. Gubbiotti, Y. M. Blanter, G. E. W. Bauer, and H. Yu, Excitation of unidirectional exchange spin waves by a nanoscale magnetic grating, *Phys. Rev. B* **100**, 104427 (2019).
- [37] K.-S. Lee, D.-S. Han, and S.-K. Kim, Physical origin and generic control of magnonic band gaps of dipole-exchange spin waves in width-modulated nanostrip waveguides, *Phys. Rev. Lett.* **102**, 127202 (2009).
- [38] A. A. Nikitin, A. B. Ustinov, A. A. Semenov, A. V. Chumak, A. A. Serga, V. I. Vasyuchka, E. Lähderanta, B. A. Kalinikos, and B. Hillebrands, A spin-wave logic gate based on a width-modulated dynamic magnonic crystal, *Appl. Phys. Lett.* **106**, 102405 (2015).
- [39] A. Khitun, Multi-frequency magnonic logic circuits for parallel data processing, *J. Appl. Phys.* **111**, 054307 (2012).
- [40] A. V. Chumak, A. A. Serga, and B. Hillebrands, Magnonic crystals for data processing, *J. Phys. D: Appl. Phys.* **50**, 244001 (2017).
- [41] Q. H. Wang *et al.*, and The magnetic genome of two-dimensional van der Waals materials, *ACS Nano* **16**, 6960 (2022).
- [42] C. Tang, L. Alahmed, M. Mahdi, M. Xiong, J. Inman, N. J. McLaughlin, Ch. Zollitsch, T. H. Kim, C. R. Du, H. Kurebayashi, E. J. G. Santos, W. Zhang, P. Li, and W. Jin, Spin dynamics in van der Waals magnetic systems, [arXiv:2301.09822](https://arxiv.org/abs/2301.09822).
- [43] S. Mandal, L. N. Kapoor, S. Ghosh, J. Jesudasan, S. Manni, A. Thamizhavel, P. Raychaudhuri, V. Singh, and M. M. Deshmukh, Coplanar cavity for strong coupling between photons and magnons in van der Waals antiferromagnet, *Appl. Phys. Lett.* **117**, 263101 (2020).
- [44] I. W. Haygood, M. R. Pufall, E. R. J. Edwards, J. M. Shaw, and W. H. Rippard, Strong coupling of an Fe-Co alloy with ultralow damping to superconducting co-planar waveguide resonators, *Phys. Rev. Appl.* **15**, 054021 (2021).
- [45] P. G. Baity, D. A. Bozhko, R. Macêdo, W. Smith, R. C. Holland, S. Danilin, V. Seferai, J. Barbosa, R. R. Peroor, S. Goldman, U. Nasti, J. Paul, R. H. Hadfield, S. McVitie, and M. Weides, Strong magnon-photon coupling with chip-integrated YIG in the zero-temperature limit, *Appl. Phys. Lett.* **119**, 033502 (2021).
- [46] Q. Xu, H. F. H. Cheung, D. S. Cormode, T. O. Puel, H. Yusuf, M. Chilcote, M. E. Flatté, E. Johnston-Halperin, and G. D. Fuchs, Strong photon-magnon coupling using a lithographically defined organic ferrimagnet, [arXiv:2212.04423](https://arxiv.org/abs/2212.04423).
- [47] S. Guo, D. Russell, J. Lanier, H. Da, P. C. Hammel, and F. Yang, Strong on-chip microwave photon-magnon coupling using ultralow-damping epitaxial $\text{Y}_3\text{Fe}_5\text{O}_{12}$ films at 2 K, *Nano Lett.* **23**, 5055 (2023).

- [48] B. Saparov and D. B. Mitzi, Organic-inorganic perovskites: Structural versatility for functional materials design, *Chem. Rev.* **116**, 4558 (2016).
- [49] A. A. Nugroho, Z. Hu, C. Y. Kuo, M. W. Haverkort, T. W. Pi, D. Onggo, M. Valldor, and L. H. Tjeng, Cross-type orbital ordering in the layered hybrid organic-inorganic compound $(\text{C}_6\text{H}_5\text{CH}_2\text{CH}_2\text{NH}_3)_2\text{CuCl}_4$, *Phys. Rev. B* **94**, 184404 (2016).
- [50] K.-Y. Kim, G. Park, J. Cho, J. Kim, J.-S. Kim, J. Jung, K. Park, C.-Y. You, and I.-H. Oh, Intrinsic magnetic order of chemically exfoliated 2D ruddlesden-popper organic-inorganic halide perovskite ultrathin films, *Small* **16**, 2005445 (2020).
- [51] R. D. Willett, C. J. Gómez-García, and B. Twamley, Long-range order in layered perovskite salts - structure and magnetic properties of $[(\text{CH}_3)_2\text{CHCH}_2\text{NH}_3]_2\text{CuX}_4$ ($X = \text{Cl}, \text{Br}$), *Eur. J. Inorg. Chem.* **2012**, 3342 (2012).
- [52] L. J. De Jongh, W. D. Van Amstel, and A. R. Miedema, Magnetic measurements on $(\text{C}_2\text{H}_5\text{NH}_3)_2\text{CuCl}_4$: ferromagnetic layers coupled by a very weak antiferromagnetic interaction, *Physica* **58**, 277 (1972).
- [53] F. Keffer and C. Kittel, Theory of antiferromagnetic resonance, *Phys. Rev.* **85**, 329 (1952).
- [54] T. Moriya, Anisotropic superexchange interaction and weak ferromagnetism, *Phys. Rev.* **120**, 91 (1960).
- [55] P. Bloembergen, P. J. Berkhout, and J. J. M. Franse, Static magnetic torque measurements on a system of ferromagnetic layers, coupled by feeble antiferromagnetic interactions; weak ferromagnetic behaviour, *AIP Conf. Proc.* **10**, 1598 (1973).
- [56] A. N. Bogdanov, A. V. Zhuravlev, and U. K. Rößler, Spin-flop transition in uniaxial antiferromagnets: Magnetic phases, reorientation effects, and multidomain states, *Phys. Rev. B* **75**, 094425 (2007).
- [57] A. H. Comstock, C.-T. Chou, Z. Wang, T. Wang, R. Song, J. Sklenar, A. Amassian, W. Zhang, H. Lu, L. Liu, M. C. Beard, and D. Sun, Hybrid magnonics in hybrid perovskite antiferromagnets, *Nat. Commun.* **14**, 1834 (2023).
- [58] T. Makihara, K. Hayashida, G. T. Noe II, X. Li, N. M. Peraca, X. Ma, Z. Jin, W. Ren, G. Ma, I. Katayama, J. Takeda, H. Nojiri, D. Turchinovich, S. Cao, M. Bamba, and J. Kono, Ultrastrong magnon-magnon coupling dominated by antiresonant interactions, *Nat. Commun.* **12**, 3115 (2021).
- [59] G. M. Diederich, J. Cenker, Y. Ren, J. Fonseca, D. G. Chica, Y. J. Bae, X. Zhu, X. Roy, T. Cao, D. Xiao, and X. Xu, Tunable interaction between excitons and hybridized magnons in a layered semiconductor, *Nat. Nanotechnol.* **18**, 23 (2023).
- [60] N. J. Lambert, J. A. Haigh, S. Langenfeld, A. C. Doherty, and A. J. Ferguson, Cavity-mediated coherent coupling of magnetic moments, *Phys. Rev. A* **93**, 021803(R) (2016).
- [61] J. Xu, C. Zhong, X. Han, D. Jin, L. Jiang, and X. Zhang, Coherent gate operations in hybrid magnonics, *Phys. Rev. Lett.* **126**, 207202 (2021).
- [62] Y. Li, V. G. Yefremenko, M. Lisovenko, C. Trevillian, T. Polakovic, T. W. Cecil, P. S. Barry, J. Pearson, R. Divan, V. Tyberkevych, C. L. Chang, U. Welp, W.-K. Kwok, and V. Novosad, Coherent coupling of two remote magnonic resonators mediated by superconducting circuits, *Phys. Rev. Lett.* **128**, 047701 (2022).
- [63] C. W. Zollitsch, S. Khan, N. V. T. Trung, I. A. Verzhbitskiy, D. Sagkovits, J. O'Sullivan, O. W. Kennedy, M. Strungaru, E. J. G. Santos, J. J. L. Morton, G. Eda, and H. Kurebayashi, Probing spin dynamics of ultra-thin van der Waals magnets via photon-magnon coupling, *Nat. Commun.* **14**, 2619 (2023).
- [64] E. Easy, Y. Gao, Y. Wang, D. Yan, S. M. Gousheghir, E.-H. Yang, B. Xu, and X. Zhang, Experimental and computational investigation of layer-dependent thermal conductivities and interfacial thermal conductance of one- to three-layer WSe_2 , *ACS Appl. Mater. Interfaces* **13**, 13063 (2021).
- [65] A. Caretta, R. Miranti, R. W. A. Havenith, E. Rampi, M. C. Donker, G. R. Blake, M. Montagnese, A. O. Polyakov, R. Broer, T. T. M. Palstra, and P. H. M. van Loosdrecht, Low-frequency raman study of the ferroelectric phase transition in a layered CuCl_4 -based organic-inorganic hybrid, *Phys. Rev. B* **89**, 024301 (2014).
- [66] L. McKenzie-Sell, J. Xie, C.-M. Lee, J. W. A. Robinson, C. Ciccarelli, and J. A. Haigh, Low-impedance superconducting microwave resonators for strong coupling to small magnetic mode volumes, *Phys. Rev. B* **99**, 140414(R) (2019).
- [67] Y. Xiong, Y. Li, M. Hammami, R. Bidthanapally, J. Sklenar, X. Zhang, H. Qu, G. Srinivasan, J. Pearson, A. Hoffmann, V. Novosad, and W. Zhang, Probing magnon-magnon coupling in exchange coupled $\text{Y}_3\text{Fe}_5\text{O}_{12}$ /permalloy bilayers with magneto-optical effects, *Sci. Rep.* **10**, 12548 (2020).
- [68] S. Khan, O. Lee, T. Dion, C. W. Zollitsch, S. Seki, Y. Tokura, J. D. Breeze, and H. Kurebayashi, Coupling microwave photons to topological spin textures in Cu_2OSeO_3 , *Phys. Rev. B* **104**, L100402 (2021).
- [69] D. Lachance-Quirion, S. P. Wolski, Y. Tabuchi, S. Kono, K. Usami, and Y. Nakamura, Entanglement-based single-shot detection of a single magnon with a superconducting qubit, *Science* **367**, 425 (2020).
- [70] D. Xu, X.-K. Gu, H.-K. Li, Y.-C. Weng, Y.-P. Wang, J. Li, H. Wang, S.-Y. Zhu, and J. Q. You, Quantum control of a single magnon in a macroscopic spin system, *Phys. Rev. Lett.* **130**, 193603 (2023).
- [71] X. Wang, Q. Yang, L. Wang, Z. Zhou, T. Min, M. Liu, and N. X. Sun, E-field control of the RKKY interaction in $\text{FeCoB}/\text{Ru}/\text{FeCoB}/\text{PMN-PT}$ (011) multiferroic heterostructures, *Adv. Mater.* **30**, 1803612 (2018).
- [72] H. Yan, Z. Feng, P. Qin, X. Zhou, H. Guo, X. Wang, H. Chen, X. Zhang, H. Wu, C. Jiang, and Z. Liu, Electric-field-controlled antiferromagnetic spintronic devices, *Adv. Mater.* **32**, 1905603 (2020).
- [73] C. Liu, Y. Luo, D. Hong, S. S.-L. Zhang, H. Saglam, L. Y. Li, Y. and B. Fisher, J. E. Pearson, J. S. Jiang, H. Zhou, J. Wen, A. Hoffmann, and A. Bhattacharya, Electric field control of magnon spin currents in an antiferromagnetic insulator, *Sci. Adv.* **7**, eabg1669 (2021).